Cytoarchitecture and Layer Estimation in High-Resolution Neuroanatomical Images

Theodore J. LaGrow [1,*], **Michael G. Moore** [1] **Judy A. Prasad**[2], **Alexis Webber**[3], **Mark A. Davenport**[1], **and Eva L. Dyer** [1,3,*]

[1] *Georgia Institute of Technology, School of Electrical and Computer Engineering, Atlanta, GA, USA*
[2] *University of Chicago, Department of Neurobiology, Chicago, IL, USA*
[3] *Georgia Institute of Technology and Emory University, Wallace H. Coulter Department of Biomedical Engineering, Atlanta, GA, USA*

Correspondence*:
Theodore J. LaGrow, Eva L. Dyer
tlagrow@gatech.edu, evadyer@gatech.edu

ABSTRACT

A robust method for quantifying the cellular architecture (cytoarchitecture) of the brain is a requisite for differentiating brain areas, identifying neurological diseases, and modeling architectural differences across species. Current methods for characterizing cytoarchitecture and, in particular, identifying laminar (layer) divisions in tissue samples, require the expertise of trained neuroanatomists to manually annotate the various regions within each image. However, as neuroanatomical datasets grow in volume, manual annotations become inefficient, impractical, and risk the potential of biasing results. In this paper, we propose an automated framework for cellular density estimation and detection of laminar divisions within retinal and neocortical datasets. This method is based upon the use of sparse recovery methods to simultaneously denoise cellular densities and detect transitions in the density which mark the beginning and end of layers. Retinal and neocortical images are used to demonstrate the efficacy of the methods. These results demonstrate the feasibility of using automation to reveal the cytoarchitecture of neurological samples in high-resolution images.

Keywords: Cytoarchitecture estimation, sparse approximation, inhomogeneous Poisson processes, total-variation minimization, group-sparse regularization, image segmentation

1 INTRODUCTION

Scientists have long been fascinated by the brain's structure and organization, prompting the development of various methods to identify the brain's many divisions and subregions (Meynert, 1868; Flechsig, 1898; Campbell, 1903; Smith, 1907). Approaches for characterizing the brain's organization were continuously refined using a variety of empirical methods until Korbinian Brodmann used both functional and pathological criteria for delineating cortical areas. Studying a range of mammalian specimens, Brodmann identified over 50 cortical structures by leveraging the distribution and packing of cells (cytoarchitecture) (Brodmann, 1909). Modeling the cytoarchitecture of the nervous system remains an area of immense focus to this day (Petrides, 2013; Weiner et al., 2017; Wagstyl et al., 2018).

A key characteristic of the cytoarchitecture of many biological tissues, including the cerebral cortex (Belgard et al., 2011) and the retina (Wandell, 1995), is the organization of the tissues into distinct layers or "lamina". In the neocortex there are six lamina, each consisting of distinct cell types and densities of

cells (Belgard et al., 2011). In the retina there are three distinct layers: the ganglion, the inner nuclear, and the outer nuclear (Chang et al., 2007). Developing a standard framework to characterize laminar cytoarchitecture can help distinguish different brain regions and quantify disease states (Chang et al., 2007).

Currently, the standard method of annotating the cytoarchitecture of a given photomicrograph (image) of the central nervous system (CNS) relies on trained neuroanatomists to inscribe neural structures and quantify regions along a given sample (Gurcan et al., 2009). The rate at which an experimentalist can provide an output is restricted by their ability to annotate large volumes of data, resulting in a potentially debilitating bottleneck to a given study. The capacity to utilize this manual annotation method to produce accurate and unbiased quantitative estimates from a sample becomes increasingly difficult as imaging techniques continue to produce datasets at larger volumes. As laboratories continue to generate larger neuroanatomical datasets, robust and automated methods are needed to find patterns in the cytoarchitecture and estimate layer transitions within the images.

In this paper, we present an automated framework for the estimation of the laminar distribution of biological tissue samples directly from microscopy images. We demonstrate an end-to-end approach that starts with raw image data to produce estimates of cellular density that can be efficiently and reliably compared. The method proposed for cellular density estimation is based upon forming a sparse representation of the underlying density function with respect to a Poisson model of the cell counts. Due to the piecewise-structure of the data, we are able to leverage fast methods for Total Variation (TV)-minimization (Rudin et al., 1992; Krahmer et al., 2017) to perform density estimation. This method uses sparse regularization to effectively find layers in tissues, resulting in the formation of compact descriptions of cellular densities. Noticing the high correlation of estimated rates in close proximity of each other, we further demonstrate feasibility of using a "group-sparse" penalty with TV (Huang et al., 2011) to group together neighboring sparse estimates. Joint regularization across many nearby patches with group sparsity can thus be used to increase the accuracy of the estimated layer transitions in a given sample. By utilizing the proposed methods of patch extraction, cell detection, and density estimation in this framework, we are able to robustly estimate the laminar distribution of biological tissue samples.

The framework proposed is applied to both retinal and neocortical photomicrographs and synthetic datasets, including a retinal tissue sample (Chang et al., 2007), Nissl-stained images from the Allen Institute for Brain Science (AIBS)'s Reference Atlas (Dong, 2008), and synthetic densities based upon laminar estimates from somatosensory and visual cortex (Gonchar et al., 2008; Meyer et al., 2010). By leveraging both a robust cell detection method and state-of-the-art density estimation technique, we show that the framework accurately estimates layers in high-resolution neuroanatomical images.

2 METHODS

The approach presented for density estimation consists of three main steps: (i) pulling out patches from the image data that run perpendicular to the cortical/sample surface, (ii) detecting cells in the sample and compressing these data down to spatially-distributed counts in each image patch, and (iii) estimating the density and layer transitions from the counts extracted in Steps i-ii. We provide MATLAB code and a demonstration of the framework at `github.com/nerdslab/arcade`.

2.1 Patch Extraction

The first step of the proposed framework involves extracting patches from a given sample. When cutting through a sample perpendicular to the outer membrane (surface), we observe sharp transitions in cell density, noting a transition in the cellular layers (see Fig. 1). Thus, in order to estimate layers from image

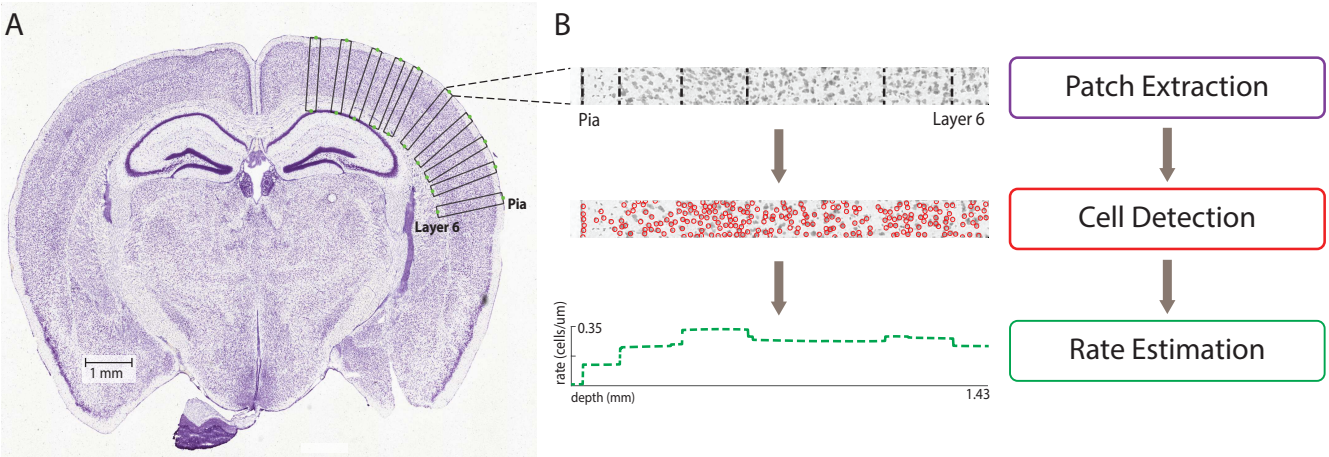

Figure 1. *Overview of the framework to estimate the cytoarchitectonics and layers in neuroanatomical images.* (A) A Nissl-stained image from the Allen Institute for Brain Science (AIBS)'s Reference Atlas (Dong, 2008) with a subset of detected patches overlaid around the upper right cortical surface. (B) From top to bottom: A patch extracted from the image to visualize the cellular distribution from the top (pia) to the bottom of the cortex (Layer 6). The dashed black lines indicate the transitions between layers as identified by a neuroanatomist. Below, detected cell bodies in red overlaid on the same image patch. Finally, the estimated density function obtained with a TV-minimization approach (dashed green).

data we must first determine the normal directions to the surface of the brain before layers can be estimated from a fixed coordinate system. However, due to the curved surface of the neocortex, determining the direction normal to the surface proves difficult to estimate.

To start, we identify the sample's surface by performing a connected components analysis (Bailey and Johnston, 2007) to produce a binary image delineating the area in the image corresponding to the brain (marked 1's) and the ambient background of the image (marked 0's). When calculating the surface normals, we cannot directly take the 2D gradient of the surface, as the approximation of the outline due to the inherent biological noise around the surface skews the estimate. Therefore, we fit a smooth curve around the surface of the sample and compute the curve's gradient instead. Finally, small patches are extracted from the image that reveal the laminar architecture of the sample. In the case of the cortical sample, we split the sample into four quadrants to parallelize the patch extraction as well as to mitigate edge cases for similar quarters of the sample. As a result, we extract a collection of patches from a large coronal brain section that run perpendicular to the detected and smoothed surface of the sample.

2.2 Cell Detection

The second step of the proposed framework involves processing raw histological imaging data to produce accurate cell counts from the sample. Due to the thickness of the sections, multiple cells appear to be overlapping in the image (see Fig. 2A,B). For this reason, we cannot simply threshold the image to pull out all of the cells. Rather, we apply a method for greedy cell detection that can deal with overlapping cells that has been previously applied for for 3D X-ray neuroanatomy data (Dyer et al., 2017) and for 2D histology images (LaGrow et al., 2018) (see Fig. 2B).

2.2.1 Pixel-level Probability Maps

The method presented for cell detection starts by applying either a supervised or unsupervised method for pixel-level segmentation that converts image data into a probability map which encodes the probability that each pixel lies in either the foreground (cell) or background (see Fig. 2A, middle row).

For the supervised approach, we use the interactive segmentation tool, Ilastik (Sommer et al., 2011), to train a random forest classifier to distinguish between the binary classes. To train a classifier in Ilastik, the

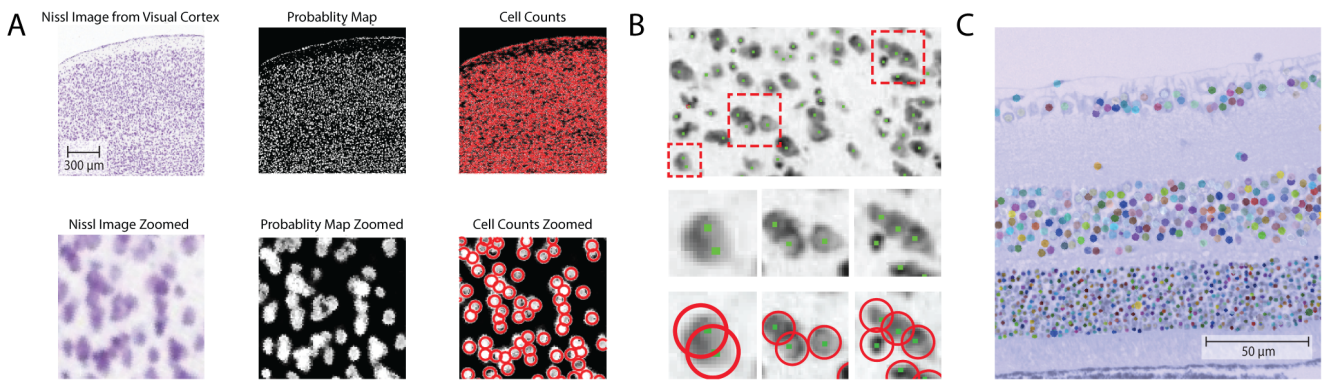

Figure 2. *Cell detection method implemented on cortical dataset and retinal dataset.* (A) A section of a Nissl-stained visual cortex image from the Allen Institute for Brian Science (AIBS)'s Reference Atlas (Dong, 2008), computed probability maps, and detected cells overlaid on the probability map (red circles) at 1.6x zoom (top row) and 12x zoom (bottom row) of the original image. (B) (top row) Demonstration of a ground truth cutout from a neocortical sample annotated by a trained neuroanatomist at 12x zoom of the original image. The green markers indicate a cell location while the dashed red boxes show examples of overlapping cells in the ground truth. (middle row) Examples of overlapping cells at 467x, 183x, and 183x zoom of the original image. (bottom row) Estimated cells (red) are overlaid on the zoomed overlapping cell examples. (C) Cell detection results overlaid on a retinal sample in a *rd10* mouse (each detected cell is displayed as a different color).

user provides a small amount of ground truth data to annotate a few examples from each class (e.g., cell or background). Ilastik leverages the use of feature selection to calculate a probability map. In the experiments on Nissl-stained cortical samples, we trained classifiers using a combination of color and intensity (Gaussian Smoothing), edge (Laplacian of Gaussian, Gaussian Gradient Magnitude, and Difference of Gaussians), and texture (Structure Tensor Eigenvalues and Hessian of Gaussian Eigenvalues) (Sommer et al., 2011).

For the unsupervised approach, we use an approach which involves fitting a Gaussian Mixture Model (GMM) to the pixel intensities in the image. GMMs are a commonly used probabilistic model that leverage the assumption that the data in question are generated from a mixture of Gaussian distributions with unknown parameters (Reynolds, 2009). The GMM method is capable of estimating the binary pixel-level class probabilities without training data. Both supervised and unsupervised methods demonstrate feasible generations of a pixel-level probability maps.

2.2.2 Iterative Cell Detection

Once the probability maps are generated with either the supervised or unsupervised approach (depending on access to training data for the specific approach), we apply a method for cell detection that employs a circular template of a fixed size to iteratively parse the probability map and produce the cell counts and location within the image (LaGrow et al., 2018; Dyer et al., 2017). The general shape of cell bodies are circular in cortical Nissl stained imaging (García-Cabezas et al., 2016). Once the point which maximally correlates to the circular template is found, we set the corresponding pixels around the point as background so the corresponding pixels do not influence future iterations (Fig. 2A). The algorithm iteratively continues to search for cells with maximum correlation until a stopping criterion is reached to account for overlapping cells. The output of the algorithm is a vector with the coordinates of the centers of the detected cells (see Fig. 2C overlaid on the original image).

Since this cell detection method is iterative in nature and thus scales with the number of cells, high-resolution and large-scale images are split into multiple sections and processed in parallel for more efficient

results. Once all of the sections are finished running, blocks of cell estimates are merged to produce the fully predicted map of cells.

2.3 Density Estimation

The third step of the proposed framework is to obtain a density function that approximates the count data from a given image patch. A simple approach for estimating the density would entail binning up the space and counting the number of cells in each bin (Simonoff and Udina, 1997). However, this histogram-based approach can be susceptible to noise and does not exploit additional information known about the laminar organization of the tissue. Thus, we leverage the fact that the layering structure of biological tissue can be modeled by a piecewise-constant density function to find efficient representations of cellular densities.

2.3.1 Density Estimation for Inhomogeneous Poisson Processes

To model the cell density in a patch of tissue as a function of the depth, we divide the space into M disjoint depth intervals and model the number of cells in each interval as a Poisson random variable, where $z_m \sim \text{Poisson}(R_m)$ denotes the number of cells observed in the mth bin and R_m denotes the density (rate) of the mth bin. We focus on a linear model where the density can be expressed as a linear combination of elements from a known basis $\boldsymbol{A}$ as $R_m^{(\boldsymbol{x})} = [\boldsymbol{A}\boldsymbol{x}]_m$, where $\boldsymbol{A}$ is a $M \times N$ matrix containing N basis elements each of M dimensions and $\boldsymbol{x} \in \mathbb{R}^N$. Under this model, the negative log-likelihood of observing $\boldsymbol{z}$ is given by

$$\mathcal{L}(\boldsymbol{z}|\boldsymbol{x}) = \mathbf{1}^T \boldsymbol{A}\boldsymbol{x} - \boldsymbol{z}^T \log(\boldsymbol{A}\boldsymbol{x}),$$

where $\boldsymbol{z} = [z_1, \ldots, z_M]$ contains the number of cells in each bin and the logarithm is applied element-wise to $\boldsymbol{A}\boldsymbol{x}$.

Note that if $\boldsymbol{A} = \boldsymbol{I}$, this model corresponds precisely to the simple binning approach described above, with $\boldsymbol{x}$ providing the corresponding bin counts. In general, however, one could choose $\boldsymbol{A}$ in a variety of more clever ways to incorporate additional structure. For example, one could allow M to be very large (i.e., binning the space at a high resolution), but avoid the sensitivity to noise this approach would normally exhibit by keeping N small and choosing $\boldsymbol{A}$ to enforce a degree of smoothness across bins. Alternatively, one could design an $\boldsymbol{A}$ where N is very large, but where we can expect $\boldsymbol{x}$ to be relatively sparse, so that it can still be accurately estimated from the noisy observations.

2.3.2 Maximum Likelihood Estimation with Total Variation Regularization

Estimating the density function $R_m^{(\boldsymbol{x})}$ typically involves solving a MLE problem to find the parameters $\boldsymbol{x}$ that best match the observed counts $\boldsymbol{z}$. However, when dealing with noisy biological data, applying additional regularization to the estimation problem helps to mitigate overfitting.

In particular, we can model the distribution of cells across cortical and retinal samples as a piecewise-constant function, where each layer is assumed to have nearly constant density (Belgard et al., 2011). In most cases, we have strong prior information about the specific number of layers and that the number of layers K is small relative to the number of bins M used to discretize the sample, i.e., $K \ll M$. Using this information, we can thus pose the density estimation problem as the following convex optimization problem:

$$\arg\min_{\boldsymbol{x}} \ \mathcal{L}(\boldsymbol{z}|\boldsymbol{x}) + \lambda \|\boldsymbol{x}\|_{\text{TV}}, \tag{1}$$

where $\|\boldsymbol{x}\|_{\text{TV}} = \sum_m |[\boldsymbol{A}\boldsymbol{x}]_{m+1} - [\boldsymbol{A}\boldsymbol{x}]_m|$ is referred to as the "total variation" (TV)-norm (Rudin et al., 1992) in the basis $\boldsymbol{A}$.

Algorithm 1 Poisson MLE with TV penalty

Require: $\boldsymbol{x} : \boldsymbol{A}\boldsymbol{x} \geq 0, \epsilon \geq 0, \alpha > 0$
  repeat
    $\boldsymbol{V} = \mathrm{diag}(\boldsymbol{A}\boldsymbol{x} + \epsilon)^{-1}\boldsymbol{A}$
    $\boldsymbol{\Lambda} = \mathrm{diag}(|\boldsymbol{D}\boldsymbol{A}\boldsymbol{x}| + \epsilon)^{-1}$
    $\boldsymbol{f} = \boldsymbol{A}^T\boldsymbol{1} - \boldsymbol{V}^T\boldsymbol{z} + \lambda\boldsymbol{A}^T\boldsymbol{D}^T\boldsymbol{\Lambda}\boldsymbol{D}\boldsymbol{A}\boldsymbol{x}$ — *majorizer gradient*
    $\boldsymbol{H} = \boldsymbol{V}^T\,\mathrm{diag}(\boldsymbol{z})\boldsymbol{V} + \lambda\boldsymbol{A}^T\boldsymbol{D}^T\boldsymbol{\Lambda}\boldsymbol{D}\boldsymbol{A}$ — *majorizer Hessian*
    $\alpha = \alpha/4$
    repeat
      $\alpha = 2\alpha$
      $\boldsymbol{y} = \boldsymbol{x} - (\boldsymbol{H} + \alpha\boldsymbol{I})^{-1}\boldsymbol{f}$ — *regularized Newton step*
    until $\boldsymbol{A}\boldsymbol{y} \geq 0$
    $\boldsymbol{x} = \boldsymbol{y}$
  until converged

When used with the TV-norm, the regularization parameter λ controls the piecewise-flatness of the resulting estimate, with larger λ will producing fewer transitions. By modulating λ, we can achieve an estimate that contains the correct number of layers in a given sample.

2.3.3 Poisson TV-Sparse Algorithm

To solve the objective in (1), we employ a majorization-minimization strategy (see Algorithm 1). Majorization-minimization allows us to replace the non-differentiable total variation term with a differentiable upper bound. This allows us solve the problem via a simple iterative method, such as Newton's method.

The majorizer we use for the total variation (in basis $\boldsymbol{A}$) is

$$\|\boldsymbol{x}\|_{\mathrm{TV}} = \|\boldsymbol{D}\boldsymbol{A}\boldsymbol{x}\|_1 \leq \frac{1}{2}\|\boldsymbol{\Lambda}^{1/2}_{(\boldsymbol{D}\boldsymbol{A}\boldsymbol{x}')}\boldsymbol{D}\boldsymbol{A}\boldsymbol{x}\|_2^2 + \frac{1}{2}\,\mathrm{Tr}(\boldsymbol{\Lambda}^{-1}_{(\boldsymbol{D}\boldsymbol{A}\boldsymbol{x}')}) \tag{2}$$

where $[\boldsymbol{D}\boldsymbol{A}\boldsymbol{x}]_m = [\boldsymbol{A}\boldsymbol{x}]_{m+1} - [\boldsymbol{A}\boldsymbol{x}]_m$ (i.e., $\boldsymbol{D}$ is $(M-1) \times M$ and has -1 along the main diagonal and $+1$ along the first superdiagonal), diagonal matrix $[\boldsymbol{\Lambda}_{(\boldsymbol{y})}]$ has entries $[\boldsymbol{\Lambda}_{(\boldsymbol{y})}]_{mm} = |\boldsymbol{y}_m|^{-1}$, and $\boldsymbol{x}'$ is any vector of the proper size ($\boldsymbol{x}$ from the previous iteration, in the algorithm). The parameter ϵ is chosen to be small and non-zero to condition the majorization, preventing singularities but otherwise having a negligible effect on the solution. The factor α is automatically tuned so that convergence is fast while accounting for the possibility of succeeding iterations estimating non-negative densities. The following reasonable initializations were used: $\epsilon = 10^{-6} \cdot max(\boldsymbol{z})$ and $\alpha = 1$. Since the application uses banded matrices for both $\boldsymbol{A}$ and $\boldsymbol{D}$, $\boldsymbol{H}$ is also a banded matrix and the linear system $(\boldsymbol{H} + \alpha\boldsymbol{I})^{-1}\boldsymbol{f}$ in Algorithm 1 can be solved efficiently – the complexity of the iteration is linear in M.

2.3.4 Group-Sparse Penalties for Spatial Regularization

The layering structure remains relatively constant within a specific neocortical region (Amunts and Zilles, 2015). This suggests that we can potentially improve the layer estimates by using the fact that nearby patches have similar layering properties when estimating layer transitions during the density estimation process. To leverage spatial similarity between patches, we will need to extend the framework to jointly estimate the density of many patches simultaneously. Suppose $\boldsymbol{X}$ and $\boldsymbol{Z}$ are obtained by stacking the patches of $\boldsymbol{x}^{(p)}$ and $\boldsymbol{z}^{(p)}$ into their columns, where $\boldsymbol{x}^{(p)}$ and $\boldsymbol{z}^{(p)}$ corresponds to the coefficients and observations of the pth patch, respectively. The likelihood of the density of patch p is simply $\mathcal{L}(\boldsymbol{z}^{(p)}|\boldsymbol{x}^{(p)})$.

Each column (patch) within $\boldsymbol{Z}$ is independent and the total negative log-likelihood is

$$\mathcal{L}(\boldsymbol{Z}|\boldsymbol{X}) = \sum_{p=1}^{P} \mathcal{L}(\boldsymbol{z}^{(p)}|\boldsymbol{x}^{(p)}). \tag{3}$$

A way to extend the independent TV framework to the multi-patch case is by using the notion of group sparsity (Huang et al., 2011). With group sparsity, we can impose the assumption that layer transitions for nearby patches should happen at the same depths. This is done by sub-additively combining (e.g., via root-sum-of-squares) the variation from multiple patches (at a single depth) before summing over depths to get the total variation. Since the inter-patch consolidation is sub-additive, there is a discount for changing multiple patches at the same depth; grouped patches are encouraged to agree on layer transitions. The penalty function we utilize is

$$\|\boldsymbol{X}\|_{\text{GTV}} = \sum_{m=1}^{M-1} \sqrt{\sum_{p=1}^{P} \left([\boldsymbol{A}\boldsymbol{x}^{(p)}]_{m+1} - [\boldsymbol{A}\boldsymbol{x}^{(p)}]_m\right)^2}. \tag{4}$$

Note that, when considering $P = 1$ patches, this reduces to the TV penalty discussed previously in (2).

While leveraging a group-TV penalty may appear substantially more complicated than the program outlined in (1), the resulting program can be managed by a nearly-identical algorithm by modifying a few definitions. The majorizer used for (4) is

$$\|\boldsymbol{X}\|_{\text{GTV}} \leq \frac{1}{2}\|\boldsymbol{\Lambda}^{1/2}_{P(\boldsymbol{D}_P\boldsymbol{A}_P\boldsymbol{X}')}\boldsymbol{D}_P\boldsymbol{A}_P\boldsymbol{X}\|_2^2 + \frac{1}{2}\operatorname{Tr}(\boldsymbol{\Lambda}^{-1}_{P(\boldsymbol{D}_P\boldsymbol{A}_P\boldsymbol{X}')}). \tag{5}$$

The difference matrix and basis matrix are given by the Kronecker products $\boldsymbol{D}_P = \boldsymbol{I}_P \otimes \boldsymbol{D}$ and $\boldsymbol{A}_P = \boldsymbol{I}_P \otimes \boldsymbol{A}$, where $\boldsymbol{I}_P$ is the $P \times P$ identity matrix. Define

$$[\boldsymbol{\Lambda}'_{(\boldsymbol{Y})}]_{mm} = \left(\sum_{p=1}^{P} [\boldsymbol{y}^{(p)}]_m^2\right)^{-\frac{1}{2}}, \tag{6}$$

and let $\boldsymbol{\Lambda}_{P(\boldsymbol{Y})} = \boldsymbol{I}_P \otimes \boldsymbol{\Lambda}'$, meaning the same coefficient is applied to $[\boldsymbol{D}\boldsymbol{A}\boldsymbol{x}^{(p)}]_m$ at each patch p, but still differs by depth m. By replacing the corresponding substitutions to Algorithm 1 for $\boldsymbol{Z}$, $\boldsymbol{X}$, $\boldsymbol{A}$, $\boldsymbol{D}$, $\boldsymbol{\Lambda}$, the resulting program will perform a group-TV-regularized Poisson maximum-likelihood estimation across multiple patches. By leveraging additional information of neighboring patches, we are able to more robustly estimate layer transitions, especially in the presence of noisy data within the image.

2.4 Model Selection and Parameter Optimization

Using manual annotations of cell locations (marked using the program ITK-Snap (Yushkevich et al., 2006), see Fig. 2B), we developed a hyper-parameter optimization method to ensure that the cell detection method selects the best set of parameters to find cells within the image. These parameters include: the initial threshold applied to the probability map, size of circular template, size of circular window used when removing a cell from the probability map, and the stopping criterion for maximum correlation of the circular template within the image. To solve the TV-minimization program, we fixed a value of λ, compute the number of transitions (number of nonzeros in x), and the value of λ increases if the number of transitions

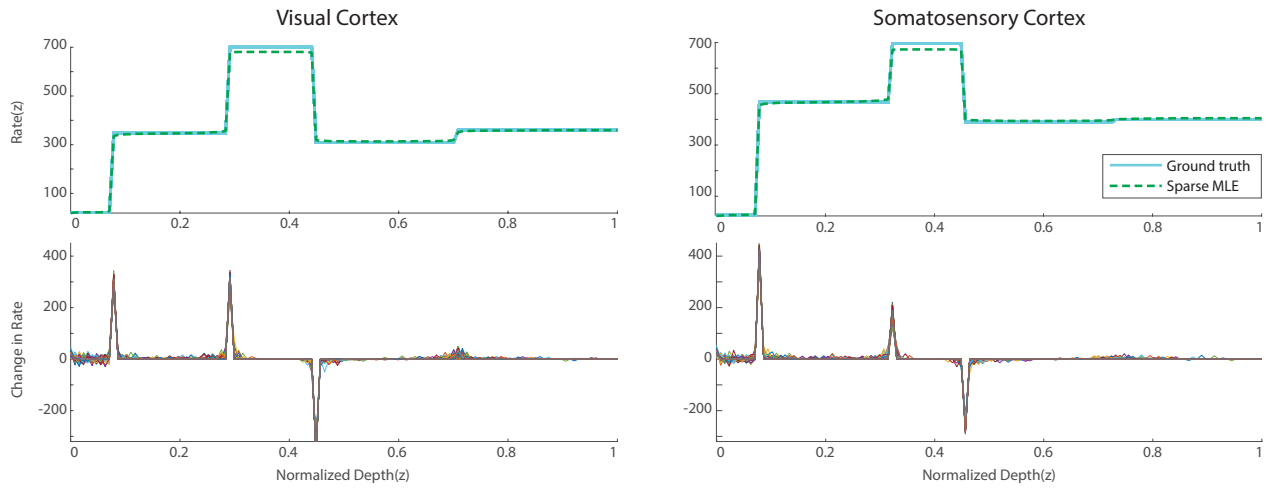

Figure 3. *Demonstration of the cytoarchitecture estimation framework on synthetic examples.* Synthetic cell density representations of noisy data modeled from visual cortex (left) and somatosensory cortex (right). From top to bottom: normalized density function for each cortical region (cyan) and density estimation using a sparse MLE with TV-minimization (dashed green); coefficients obtained under a sparse MLE model elucidating sparse layer transitions as measured by the total-variation norm (50 trials).

does not match the user input. We repeat this until an appropriate λ is chosen to achieve the desired number of layers, using the solution from the previous value of λ as a warm start.

After estimating the coefficients, we often observe that transitions in density are smooth and thus produce a series or cluster of coefficients. Therefore, to indicate the transition in this case, we filter the coefficients to find local maxima and suppress the residual coefficients in a neighborhood around the maximum value. To filter the sparse coefficients, we threshold and apply a peak detector to prune the coefficients obtained through the TV-minimization method. Thereby, we are able to constrain the resulting coefficients significantly to produce an estimate with the specified number of transitions.

3 RESULTS

The proposed cell detection and density estimation methods were tested on two distinct neuroanatomical datasets. The first dataset was obtained from a Nissl-stained cortical section from the AIBS's Reference Atlas (Fig. 2A,B) (Dong, 2008). The second sample was obtained from a retinal tissue section stained with toluidine blue (Fig. 2C). Both the cortical and retinal samples exemplify the layer-specific structure assumed in the framework.

To demonstrate efficacy, we started by testing the cell detection approach. To do this, we extracted a small 300×300 pixel cutout (295 μm x 295 μm) from the retinal and cortical samples and manually annotated the center of the cells in the cutout using ITK-Snap (Yushkevich et al., 2006). We then optimized the hyper-parameters used in the cell detection method to maximize the f1-score (harmonic mean of precision and recall) for the cutout. When we tested the cell detection method on a new cortical sample and the supervised classifier (random forest classifier; Ilastik) generated a f1-score of 0.903 and the unsupervised case (GMM) generated an f1-score of 0.925. Following, we executed a new run of the cell detection methods on a retinal sample which consists of heterogeneous cell types of different sizes. We split the sample into two parts and applied the cell detection method to find cells of the two different sizes. The supervised classifier generated a f1-score of 0.920 for the first two layers (ganglion cells, inner nuclear layer) and 0.863 for the third layer (outer nuclear layer). For the unsupervised classifier (GMM), the first two layers of the retinal sample generated an f1-score of 0.983 and the third layer generated an f1-score of

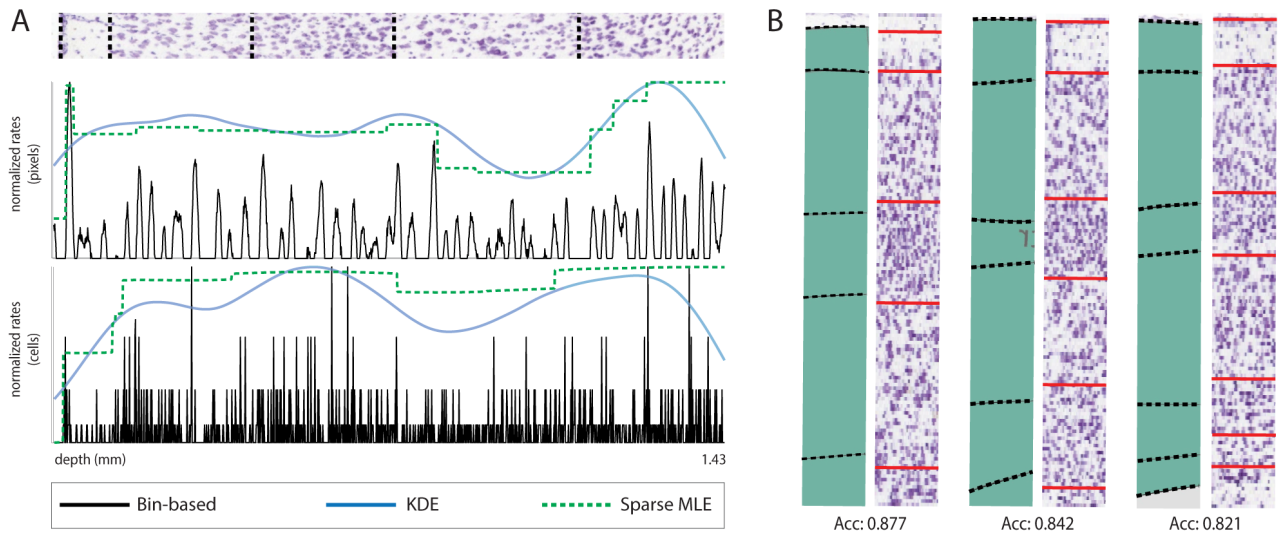

Figure 4. *Demonstration of density estimation.* (A) (top) An extracted patch from the primary somatosensory cortex (SSp) overlaid with the true annotated layer transitions in dashed black. (middle) Using pixel values, the plot indicate the optimal accuracy of the bin-based pixel values (black), the kernel density estimation of pixels (blue), and the sparse MLE of pixels (dashed green). (bottom) Using detected cell counts, the plot indicate the optimal accuracy of the bin-based cell counts (black), the kernel density estimation of cells (blue), and the sparse MLE of the cells (dashed green). The key corresponding to the patches and graphs follow below A. (B) Several additional patches compared to manual annotations from AIBS's Reference Atlas using the same parameters of optimal accuracy trained in A. The accuracy of the layer transitions is displayed below each patch.

0.886. The results suggest that the cell detection methods can reliably detect cells from both retinal and cortical datasets.

To test the proposed TV-minimization approach for density estimation and layer estimation, we initially generated two synthetic datasets that authentically modeled cellular densities in both the primary somatosensory cortex (SSp) and the primary visual cortex (VISp) in the neocortex of the brain (Dong, 2008; Gonchar et al., 2008; Meyer et al., 2010) (see Fig. 3). In this case, the cortex is modeled as consisting of five layers (L1, L2/3, L4, L5, L6), each with constant density. Using this bio-realistic density function, we generated a discrete-time arrival process by drawing counts from a Poisson distribution based on either the VISp or SSp distrobution function (Fig. 3). We applied TV-regularization to encourage a piecewise-constant solution, where the non-zeros in the estimated coefficients ($\boldsymbol{x}$) correspond to the locations where each new layer begins (Fig. 3 (bottom row)). We leveraged $\boldsymbol{A} = \boldsymbol{I}$ during the majorization-minimization step in computation. In this example, layers 2/3 are considered as one layer with constant density and thus the true solution for $\boldsymbol{x}$ is exactly 4-sparse. The final rate estimates align with the true density function. Thus, we demonstrate that the proposed method for density estimation can accurately estimate appropriate layer transitions for a bio-realistic sample.

After validating that our proposed density estimation method can be applied to synthetic data, we applied the method to individual image patches extracted from the neocortical sample (Fig. 4). We compare the layer transition estimation to both a bin-based method and a more standard method for density estimation, a kernel density estimator (KDE) which smooths the count data in the cortical sample (Silverman, 2018) (Fig. 4A). A trained neuroanatomist manually annotated layer transitions for the patches in question to validate and calculate the performance for each method. The accuracy of each comparative method was based on a spike-based metric where the spatial disparity of each transition is compared to the ground truth data (Victor, 2005). There are three steps to computing this error metric: (i) determine if the test produced the correct number of layer transitions, (ii) assign the estimated transitions to the spatially nearest ground

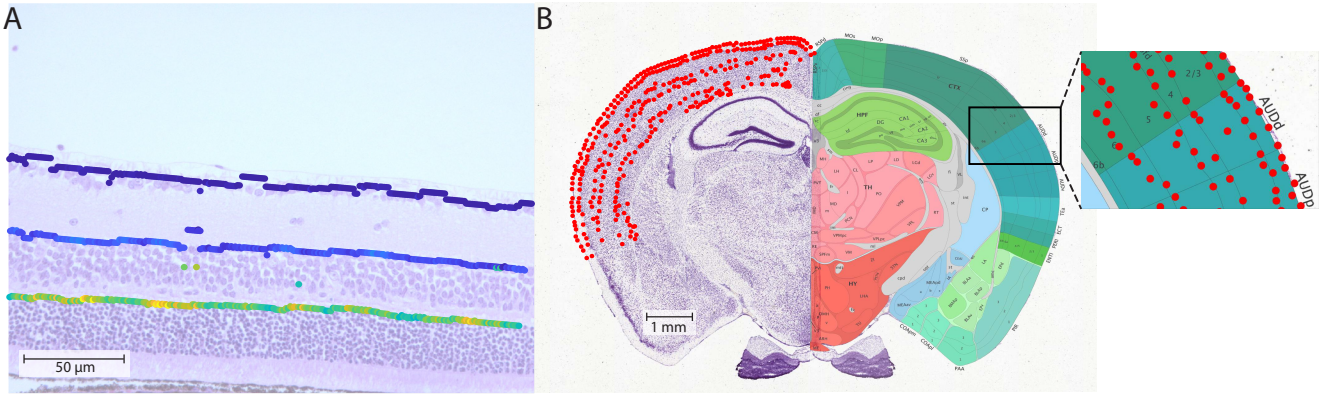

Figure 5. *Results of cytoarchitecture estimation framework on neuroanatomical images.* (A) Estimated layer transition points are colored according to their estimated rate (dark blue corresponds to low rates, bright yellow corresponds to high rates) overlaid on the retinal sample of a *rd10* mouse. (B) The right neocortical region of the Nissl-stained image mirrored with both the overlaid estimated transition points in red (left) and the AIBS's manual annotation reference atlas (right). The inlet of B depicts the transition points overlaid against the Allen Institute Reference Atlas.

truth transition, and (iii) sum the spatial pixel differences between the estimated transitions and the ground truth transitions over the length of the patch. In all of the tests, both the pixel values and detected cell counts are used to determine whether detected cells in the extracted patch added additional information when estimating the layer transitions (Fig. 4A, Table 1). The results suggest that utilizing the method of density estimation in conjunction with detected cell counts produces a more accurate outcome of layer estimation.

Method	Pixel Values	Cell Counts
Bin-based	0.612	0.694
KDE	0.790	0.865
Sparse MLE	0.822	0.914

Table 1. *Results of layer transition accuracy.* Accuracy of layer change estimation in a cortical patch against ground truth labeling from AIBS's manual annotations using a summation of either pixels or cell counts, kernel density estimation (KDE), or the sparse MLE approach.

To see whether the same parameters will produce a similar accuracy on new patches, we tested the parameters used for the patch in Fig. 4A on additional patches in the same region of the cortex (see Fig. 4B). Based on the spike-based metric of each transition compared to the the AIBS atlas (Dong, 2008), the resulting accuracy of the three additional patches were: 0.877, 0.842, and 0.821. The results demonstrate that transferring the optimal parameters from one patch to additional patches yields comparable layer transitions to the ground truth annotations provided by the AIBS atlas (Dong, 2008) (see Fig. 4B). Therefore, we are able to utilize parameters of a patch on nearby patches within a given sample. We process both the retina sample (Fig. 5A) and the left hemisphere of the cortical sample (mirrored with the corresponding AIBS's atlas annotation (Dong, 2008) in Fig. 5B), demonstrating the framework on two neuroanatomical samples.

To test the hypothesis that joint estimation should improve the accuracy of density estimates over the independent case, we incorporated a group-sparse regularization penalty into the optimization framework

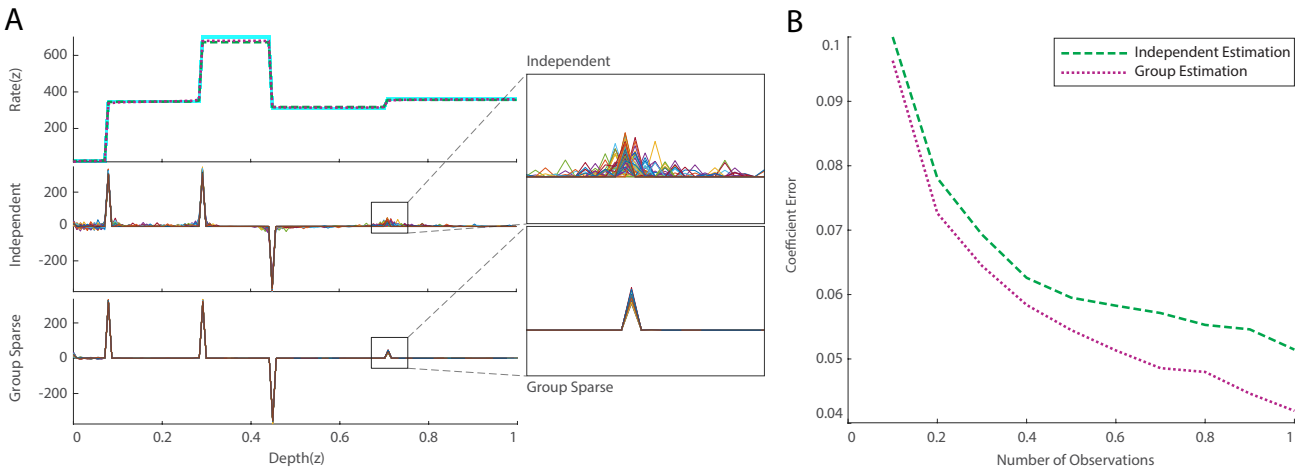

Figure 6. *Demonstration of group-sparse approximation for dealing with noisy, corrupted, or missing data.* (A) Comparison of independent and group-sparse penalty methods. (top) The normalized density function for primary visual cortex (cyan) and density estimates obtained using an independent sparse (dashed green) and group-sparse (dotted purple) model. Coefficients obtained under an (middle) independent sparse and (bottom) group-sparse model. (B) Average coefficient error as a function of the number of observations under an independent and group-sparse model in the noisy rate setting (averaged over 15 trials).

for the constrained MLE. We tested both the independent and group-sparse methods on the VISp synthetic data set to compare both method's performance drawn from a noisy version of the same underlying VISp density function (with Gaussian noise added to simulate potential artifacts). In the independent case, we estimated the density for each observation separately. In the group case, we estimated the density for all observations jointly. The results align well with the predictions: when we estimate the rates jointly we observe an improvement in performance (Fig. 6A) and when we increase the number of observations, we observe that the gap between the two methods also increases accordingly (Fig. 6B). These preliminary results suggest that group sparsity can be used to improve estimation of rates over the independent case.

4 DISCUSSION

In this paper, we introduced a framework for estimating cytoarchitecture in high-resolution neuroanatomical images. The proposed approach combines a method for cell detection with a sparse recovery-based approach for density estimation to both denoise density estimates and also estimate laminar transitions. We applied the framework to images from both retinal and neocortical samples and demonstrated that the methods are able to robustly detect cells and layer transitions.

The proposed approach for density estimation utilizes TV-regularization because the assumptions that the data consists of homogeneous regions of nearly constant density naturally fits this specific regularizer. This is but one choice of a regularizer that could be used to detect layers in histological datasets. For example, wavelets are also capable of sparsely representing density functions and promote sharp transitions in the data (Starck et al., 2010). Additionally, as we move to three dimensions, surflets (Chandrasekaran et al., 2004) could also be used to sparsely represent multidimensional density functions and promote sharp transitions in the data. By extending the method to other basis sets (beyond using TV-minimization) and to higher dimensions, the framework will increasingly be able to find transitions in densities beyond the laminar structures we considered here.

There exist a number of alternative methods for extracting layers from histology datasets. These methods typically start by smoothing the image data and fitting splines or other polynomials to identify regions

where the image contrast changes significantly. One such example leverages B-splines to parcellate layers in BigBrain, a high-resolution 3D model of a human brain (Lewis et al., 2014). Similarly, in work from Feng et al. (2016), the authors developed a method to segment brain regions and layers of the olfactory bulb using a closed cubic spline (CCS)-based approach. In contrast to these smoothing-based approaches, this proposed approach works directly on cell counts and thus solves the problem of density and layer estimation simultaneously.

In this work, we focused on the estimation of layers present within cortical and retinal samples. However, the identification of layers is just one attribute of cytoarchitecture that may be extracted using these methods. Recurring spatial patterns such as "barrels" formed by clusters of neurons within somatosensory cortex (Petersen, 2009) could theoretically also be detected using the density estimation methods we presented, however the current staining technique makes barrels hard to detect. By extending the sparse approximation framework to other staining methods and different basis sets, we can extract more complex properties of cellular architecture to delineate structures that are challenging for a novice to identify (Amunts and Zilles, 2015) (e.g., thalamic and hypothalamic nuclei).

While we focus on characterizing cytoarchitecture here, the same methods could also be applied to estimate the architecture of a wider range of neural structures in the brain. For instance, many efforts have been made to develop automated methods for detecting synapses (Li et al., 2010; Roncal et al., 2014; Anton-Sanchez et al., 2014; Domínguez-Álvaro et al., 2018), neuronal arbors (Sümbül et al., 2014), organelles (Perez et al., 2014), and spines (Anton-Sanchez et al., 2017). Thus, with very minor modifications sparse recovery-based methods could be used to quantify the architecture of these diverse neural structures when revealed by different imaging modalities like electron microscopy (Kasthuri et al., 2015) and X-ray microtomography (Dyer et al., 2017).

Using simulated data, we demonstrated that the proposed sparse recovery framework could be extended to the group-sparse case to jointly regularize density estimates across many nearby patches. This group sparsity approach could be further applied to help with the issue of missing data and noise (due to tears or bubbles in the section) by first detecting outlier patches and then filling in their density estimates to be consistent with their neighbors. Through utilizing other structured sparsity models (Baraniuk et al., 2010), we can extend this sparse recovery framework to take into account additional known structure like boundaries between areas.

Recently, new tools for quantitative mapping of cell types has revealed detailed information about the morphological characteristics (i.e., shape, size, and branching structure) of cells in different cortical layers (Zeng and Sanes, 2017). The current methods do not take into account information about the shape and size of cells, however, by utilizing tools for marked point processes (Descombes and Zerubia, 2002) each of the detected counts or cells can be associated with metadata that describes different attributes of the detected cell. Thus by extending the Poisson model to the case of marked processes, we can capture multi-dimensional characteristics of the cytoarchitecture that includes information about cell type, shape, and size.

The work we presented in this paper provides a necessary starting point for automating the process of learning cytoarchitecture from image data. As the framework continues to develop, it will be possible to model more complex patterns of cytoarchitecture in higher dimensions to find divisions between brain areas. Through automated approaches to model the architecture of the brain at multiple scales, we can further quantify changes in the cytoarchitecture due to disease (Chang et al., 2007; Hodges et al., 2006; Nobakht et al., 2011), aging (Ulrich, 1988; Roth et al., 2017), and evolution (Seelke et al., 2013).

AUTHOR CONTRIBUTIONS

TL and ED developed the framework presented in this paper and wrote the manuscript with feedback from all authors. TL conducted the experiments and analyzed the results. MM, MD, and ED developed the methods for density estimation introduced in the paper. JP designed the synthetic datasets used in this study. JP and AW annotated the ground truth of samples used in this study. All authors listed have made a substantial, direct and intellectual contribution to the work, and approved it for publication.

FUNDING

This work was supported by the National Institute of Mental Health of the National Institutes of Health under Award Number R24MH114799.

DATA AVAILABILITY STATEMENT

The datasets used in this study can be found at `github.com/nerdslab/arcade`.

REFERENCES

Amunts, K. and Zilles, K. (2015). Architectonic mapping of the human brain beyond brodmann. *Neuron* 88, 1086–1107

Anton-Sanchez, L., Bielza, C., Merchán-Pérez, A., Rodríguez, J.-R., DeFelipe, J., and Larrañaga, P. (2014). Three-dimensional distribution of cortical synapses: a replicated point pattern-based analysis. *Frontiers in neuroanatomy* 8, 85

Anton-Sanchez, L., Larrañaga, P., Benavides-Piccione, R., Fernaud-Espinosa, I., DeFelipe, J., and Bielza, C. (2017). Three-dimensional spatial modeling of spines along dendritic networks in human cortical pyramidal neurons. *PloS one* 12, e0180400

Bailey, D. G. and Johnston, C. T. (2007). Single pass connected components analysis. In *Proceedings of image and vision computing New Zealand*. 282–287

Baraniuk, R. G., Cevher, V., Duarte, M. F., and Hegde, C. (2010). Model-based compressive sensing. *IEEE Transactions on Information Theory* 56, 1982–2001

Belgard, T. G., Marques, A. C., Oliver, P. L., Abaan, H. O., Sirey, T. M., Hoerder-Suabedissen, A., et al. (2011). A transcriptomic atlas of mouse neocortical layers. *Neuron* 71, 605–616

Brodmann, K. (1909). *Vergleichende Lokalisationslehre der Grosshirnrinde in ihren Prinzipien dargestellt auf Grund des Zellenbaues* (Barth)

Campbell, A. W. (1903). Histological studies on cerebral localisation. *Proceedings of the Royal Society of London* 72, 488–492

Chandrasekaran, V., Wakin, M. B., Baron, D., and Baraniuk, R. G. (2004). Surflets: A sparse representation for multidimensional functions containing smooth discontinuities. In *Information Theory, 2004. ISIT 2004. Proceedings. International Symposium on* (IEEE), 563

Chang, B., Hawes, N., Pardue, M., German, A., Hurd, R., Davisson, M., et al. (2007). Two mouse retinal degenerations caused by missense mutations in the β-subunit of rod cgmp phosphodiesterase gene. *Vision Research* 47, 624–633

Descombes, X. and Zerubia, J. (2002). Marked point process in image analysis. *IEEE Signal Processing Magazine* 19, 77–84

Domínguez-Álvaro, M., Montero-Crespo, M., Blazquez-Llorca, L., Insausti, R., DeFelipe, J., and Alonso-Nanclares, L. (2018). Three-dimensional analysis of synapses in the transentorhinal cortex of alzheimer's disease patients. *Acta neuropathologica communications* 6, 20

Dong, H. W. (2008). *The Allen reference atlas: A digital color brain atlas of the C57Bl/6J male mouse.* (John Wiley & Sons Inc)

Dyer, E. L., Roncal, W. G., Prasad, J. A., Fernandes, H. L., Gürsoy, D., Andrade, V. D., et al. (2017). Quantifying mesoscale neuroanatomy using X-ray microtomography. *eNeuro* 4

Feng, Z., Li, A., Gong, H., and Luo, Q. (2016). An automatic method for nucleus boundary segmentation based on a closed cubic spline. *Frontiers in neuroinformatics* 10, 21

Flechsig, P. (1898). Neue untersuchungen uber die markbildung in den menschlichen grosshirnlappen. *Neurol Centribi* 17, 977–996

García-Cabezas, M. Á., John, Y. J., Barbas, H., and Zikopoulos, B. (2016). Distinction of neurons, glia and endothelial cells in the cerebral cortex: an algorithm based on cytological features. *Frontiers in neuroanatomy* 10, 107

Gonchar, Y., Wang, Q., and Burkhalter, A. H. (2008). Multiple distinct subtypes of GABAergic neurons in mouse visual cortex identified by triple immunostaining. *Frontiers in Neuroanatomy* 2, 3

Gurcan, M. N., Boucheron, L., Can, A., Madabhushi, A., Rajpoot, N., and Yener, B. (2009). Histopathological image analysis: A review. *IEEE Reviews in Biomedical Engineering* 2, 147–171

Hodges, A., Strand, A. D., Aragaki, A. K., Kuhn, A., Sengstag, T., Hughes, G., et al. (2006). Regional and cellular gene expression changes in human huntington's disease brain. *Human molecular genetics* 15, 965–977

Huang, J., Zhang, T., and Metaxas, D. (2011). Learning with structured sparsity. *Journal of Machine Learning Research* 12, 3371–3412

Kasthuri, N., Hayworth, K. J., Berger, D. R., Schalek, R. L., Conchello, J. A., Knowles-Barley, S., et al. (2015). Saturated reconstruction of a volume of neocortex. *Cell* 162, 648–661

Krahmer, F., Kruschel, C., and Sandbichler, M. (2017). Total variation minimization in compressed sensing. In *Compressed Sensing and its Applications* (Springer). 333–358

LaGrow, T. J., Moore, M. G., Prasad, J. A., Davenport, M. A., and Dyer, E. L. (2018). Approximating cellular densities from high-resolution neuroanatomical imaging data. In *Proc. 40th Annual IEEE Engineering in Medicine and Biology Conference* (Honolulu, HI)

Lewis, L., Lepage, C., Fournier, M., Zilles, K., Amunts, K., and Evans, A. C. (2014). Bigbrain: Initial tissue classification and surface extraction. In *20th Annual Meeting of the Organization for Human Brain Mapping (OHBM)*

Li, L., Tasic, B., Micheva, K. D., Ivanov, V. M., Spletter, M. L., Smith, S. J., et al. (2010). Visualizing the distribution of synapses from individual neurons in the mouse brain. *PloS one* 5, e11503

Meyer, H. S., Wimmer, V. C., Oberlaender, M., De Kock, C. P., Sakmann, B., and Helmstaedter, M. (2010). Number and laminar distribution of neurons in a thalamocortical projection column of rat vibrissal cortex. *Cerebral cortex* 20, 2277–2286

Meynert, T. (1868). *Der Bau der Gross-Hirnrinde: und seine örtlichen Verschiedenheiten, nebst einem pathologisch-anatomischen Corollarium* (Heuser)

Nobakht, M., Hoseini, S. M., Mortazavi, P., Sohrabi, I., Esmailzade, B., Roosh, N. R., et al. (2011). Neuropathological changes in brain cortex and hippocampus in a rat model of alzheimer's disease. *Iranian biomedical journal* 15, 51

Perez, A. J., Seyedhosseini, M., Deerinck, T. J., Bushong, E. A., Panda, S., Tasdizen, T., et al. (2014). A workflow for the automatic segmentation of organelles in electron microscopy image stacks. *Frontiers in neuroanatomy* 8, 126

Petersen, C. (2009). *Barrel cortex circuits.* Tech. rep., Academic Press

Petrides, M. (2013). *Neuroanatomy of language regions of the human brain* (Academic Press)

Reynolds, D. A. (2009). Gaussian mixture models. In *Encyclopedia of Biometrics*

Roncal, W. G., Pekala, M., Kaynig-Fittkau, V., Kleissas, D. M., Vogelstein, J. T., Pfister, H., et al. (2014). Vesicle: volumetric evaluation of synaptic interfaces using computer vision at large scale. *arXiv preprint arXiv:1403.3724*

Roth, W., Morgello, S., Goldman, J., Mohr, J. P., Elkind, M. S., Marshall, R. S., et al. (2017). Histopathological differences between the anterior and posterior brain arteries as a function of aging. *Stroke* , STROKEAHA–116

Rudin, L. I. et al. (1992). Nonlinear total variation based noise removal algorithms. *Physica D: Nonlinear Phenomena* 60, 259–268

Seelke, A. M., Dooley, J. C., and Krubitzer, L. A. (2013). Differential changes in the cellular composition of the developing marsupial brain. *Journal of Comparative Neurology* 521, 2602–2620

Silverman, B. W. (2018). *Density estimation for statistics and data analysis* (Routledge)

Simonoff, J. S. and Udina, F. (1997). Measuring the stability of histogram appearance when the anchor position is changed. *Computational Statistics & Data Analysis* 23, 335–353

Smith, G. E. (1907). A new topographical survey of the human cerebral cortex, being an account of the distribution of the anatomically distinct cortical areas and their relationship to the cerebral sulci. *Journal of anatomy and physiology* 41, 237

Sommer, C., Straehle, C. N., Koethe, U., and Hamprecht, F. A. (2011). Ilastik: Interactive learning and segmentation toolkit. In *IEEE International Symposium on Biomedical Imaging: From Nano to Macro*. 230–233

Starck, J.-L., Murtagh, F., and Fadili, J. M. (2010). *Sparse image and signal processing: wavelets, curvelets, morphological diversity* (Cambridge university press)

Sümbül, U., Zlateski, A., Vishwanathan, A., Masland, R. H., and Seung, H. S. (2014). Automated computation of arbor densities: a step toward identifying neuronal cell types. *Frontiers in neuroanatomy* 8, 139

Ulrich, J. (1988). *Histology and histopathology of the aging brain*, vol. 25 (S Karger Ag)

Victor, J. D. (2005). Spike train metrics. *Current opinion in neurobiology* 15, 585–592

Wagstyl, K., Lepage, C., Bludau, S., Zilles, K., Fletcher, P. C., Amunts, K., et al. (2018). Mapping cortical laminar structure in the 3d bigbrain. *Cerebral Cortex* 28, 2551–2562

Wandell, B. A. (1995). *Foundations of vision*, vol. 8 (Sinauer Associates Sunderland, MA)

Weiner, K. S., Barnett, M. A., Lorenz, S., Caspers, J., Stigliani, A., Amunts, K., et al. (2017). The cytoarchitecture of domain-specific regions in human high-level visual cortex. *Cerebral cortex* 27, 146–161

Yushkevich, P. A., Piven, J., Hazlett, H. C., Smith, R. G., Ho, S., Gee, J. C., et al. (2006). User-guided 3D active contour segmentation of anatomical structures: Significantly improved efficiency and reliability. *Neuroimage* 31, 1116–1128

Zeng, H. and Sanes, J. R. (2017). Neuronal cell-type classification: challenges, opportunities and the path forward. *Nature Reviews Neuroscience* 18, 530

CONFLICT OF INTEREST STATEMENT

The authors declare that the research was conducted in the absence of any commercial or financial relationships that could be construed as a potential conflict of interest.